THE JOURNAL OF PHYSICAL CHEMISTRY C
A JOURNAL OF THE AMERICAN CHEMICAL SOCIETY

pubs.acs.org/JPCC
Article

Anisotropic Strain Observation in Naturally Occurring Buckling on Twisted Bilayer Graphene: A Nano-Raman Study

Gustavo Soares, Rafael R. Barreto, Rafael Nadas, Kenji Watanabe, Takashi Taniguchi, Leonardo C. Campos, Luiz G. Cançado, and Angelo Malachias*

Cite This: J. Phys. Chem. C 2025, 129, 7508−7519

ABSTRACT: Twisted bilayer graphene (tBG) is an exuberant electronic system, exhibiting a wide variety of electronic behaviors intricately influenced by both the twist angle and internal built-in strain. In our study, we explore how naturally occurring variations in the mismatch angle in the bilayer graphene result in localized strain gradients. These gradients are sufficient to store elastic energy, promoting deterministic buckling phenomena. Utilizing tip-enhanced Raman spectroscopy, we conducted nanometer-scale mapping of twist angle, strain distribution, and elastic energy across tBG, identifying pronounced and deterministic fluctuations in Raman peak shifts, particularly within the 2D band on wrinkled areas. This analysis enabled us to distinguish between uniaxial and biaxial strain effects and to evaluate the elastic energy that remains within these structures. Supported by finite element modeling, our results elucidate the relationship between anisotropic strain dynamics and buckling behavior, enhancing our understanding of tBG's mechanical properties. Our findings contribute to the field of strain engineering in tBG and suggest new possibilities for tailoring the electronic and structural characteristics of these materials at the nanoscale.

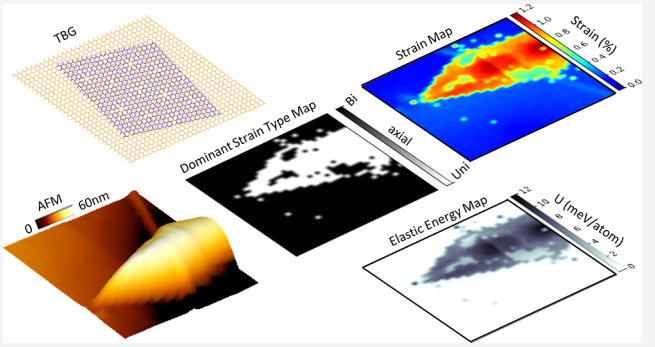

1. INTRODUCTION

Twisted bilayer graphene (tBG) has emerged as a cornerstone in condensed matter physics and materials science. This material's ability to form a periodic superlattice of electronic density (usually identified in microscopy techniques by moiré patterns) at specific "magic" angles, such as ∼1.1°, results in nearly flat electronic bands. Such condition enables the study of strongly correlated electronic phases like superconductivity, Mott insulators, and topological states.[1−5] Moreover, tBG has shown exceptional potential for thermoelectric applications, with reports of enhanced thermoelectric power factors near the magic angle due to an increase of Seebeck coefficients with consequent reduction of thermal conductivity, positioning tBG as a promising candidate for energy harvesting and related technologies.[6−10] These properties have catalyzed advancements in areas nowadays referred as twistronics and straintronics, where the twist angle between graphene layers is a crucial parameter for tuning electronic effects.[11,12] As demonstrated in waveguide-integrated devices, applications in photonics further highlight tBG's versatility by exploiting its enhanced optical absorption capabilities due to van Hove singularities at higher twist angles.[13]

Despite these advances, leveraging tBG for practical devices remains challenging. Achieving reproducibility in the precise alignment of graphene layers within a precision of fractions of a degree is an accurate process in which even slight deviations can significantly alter electronic properties.[14] Additionally, intrinsic issues like strain-induced wrinkle formation and long-range stability of interlayer bonding add complexity to the fabrication process.[11] These challenges are exacerbated when integrating tBG into functional devices, such as superconducting Josephson junctions and optoelectronic components, due to the requirement of ultraclean interfaces and precise electrostatic gating.[15]

Moreover, the incorporation of tBG into scalable technology is hindered by the need for uniformity and control of domain formation due to lattice relaxation. The limitations in device reproducibility and the high sensitivity of tBG properties to environmental factors underline the difficulties in transitioning tBG research from fundamental studies to practical applications.[14] Addressing these issues requires innovations in fabrication techniques and material engineering, particularly in controlling the moiré superlattice parameters that would diminish angle disorder.[16] These advancements will be pivotal

Received: January 22, 2025
Revised: March 9, 2025
Accepted: March 28, 2025
Published: April 5, 2025

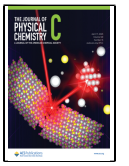

https://doi.org/10.1021/acs.jpcc.5c00506
J. Phys. Chem. C 2025, 129, 7508−7519

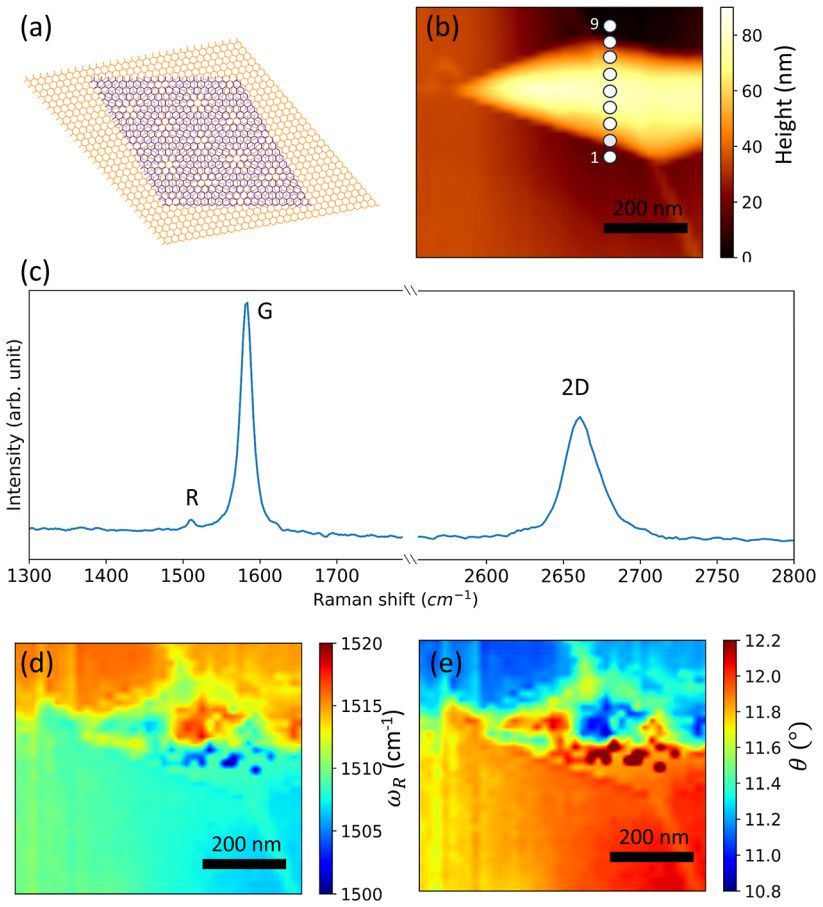

Figure 1. (a) Schematic of moiré pattern of 10° twisted bilayer graphene. (b) AFM topographic profile of a selected region with 700 × 700 nm^2 in our sample, showing a large buckled structure (wrinkle). The white dots ranging from 1 to 9 are used to indicate spectral measurements depicted in Figure 3. (c) Raman spectrum on a flat region of the tBG, showing the R (≈1518 cm^{-1}), G (≈1585 cm^{-1}), and 2D (≈2650 cm^{-1}) peaks. (d) Hyper-spectral map from TERS in the same region mapped in (b), depicting the R band peak position. (e) Map with calculated tBG angle using the iTO mode along different angles for R band peak position.

in unlocking the full potential of tBG for next-generation quantum and optoelectronic technologies.

Tip-enhanced Raman spectroscopy (TERS) has become a vital vibrational probing technique at the nanoscale, integrating the spectroscopic precision of Raman scattering with significant signal enhancement.[17−19] The efficacy of TERS is attributed to its capability to surpass the diffraction limit of light for spatial resolution, combined with an enhanced sensitivity inherent to Raman spectroscopy. This synergy allows for the nanoimaging of single molecules, establishing TERS as an indispensable tool in fields such as chemistry, biology, and materials science.[20−22] In our study, we utilized local near-field Raman measurements and finite element method simulations to assess the strain and elastic energy in twisted bilayer graphene (tBG).

We fabricated the tBG using a transfer system to set a mismatch angle of 10°, which was characterized via Raman spectroscopy. Employing TERS, we achieved high spatial resolution mapping of the sample, identifying wrinkled regions confirmed by topographic images. Hyperspectral mapping enabled us to observe variations in the two-phonon totally symmetric transversal optical 2D band (∼2650 cm^{-1})[23] specifically in areas with wrinkles. By analyzing shifts in the 2D band, we directly quantified the local strain in these regions. We observed a splitting of the 2D band inside the wrinkled region, with the appearance of a new peak. Such features allow us to distinguish between uniaxial and biaxial strain. Our results reveal that anisotropic strain conditions generate localized gradients with sufficient energy to create buckled areas. Elasticity parameters used along tBG data analysis in this work, known to be slightly different from those of monolayer graphene, are verified by finite element method (FEM) simulations of wrinkle morphologies. The elastic energy inside wrinkled regions is then evaluated and exceeds the adhesion energy between the graphene layers and the substrate. Our approach provides a comprehensive understanding of the inherent mechanical behavior of tBG under strain, offering insights into the potential for strain engineering in the development of processes that can lead to tBG-based devices.

2. EXPERIMENTAL METHODS

Twisted bilayer graphene samples were fabricated to achieve specific optical absorption resonance angles, using the tear-and-stack method described in ref 16. First, graphene flakes were initially isolated via micromechanical exfoliation onto a 300 nm-thick thermally grown oxide layer on a SiO_2/Si substrate. The exfoliated graphene sheet was torn into two-halves. One-half was carefully transferred and aligned with an in-plane misorientation angle (θ) of around 10° atop the remaining half. This stacking creates a θ-dependent electronic density pattern (moiré pattern) due to atomic superposition in some regions.[24−26] Finally, the tBG was transferred to a hexagonal boron nitride (hBN) flake centered on top of a covered glass substrate.

https://doi.org/10.1021/acs.jpcc.5c00506
J. Phys. Chem. C 2025, 129, 7508−7519

Raman spectroscopy was employed for the systematic characterization of three different graphene systems: monolayer graphene, bilayer graphene, and twisted bilayer graphene (tBG). In tBG, the tuning of energy between van Hove singularities and the incident laser photon energy was adjusted to enhance the absorption probability,[27−29] resulting in an increase of the G band intensity by up to 12.5 times compared to typical bilayer graphene under similar laser power conditions. Another notable feature in the tBG system is the emergence of the R band adjacent to the G band, attributed to the θ-dependent phonon activation induced by the unique moiré geometry.[29,30]

TERS analyses were carried out using a FabNS Porto-SNOM system, employing an oil-immersion objective lens with a numerical aperture of 1.4 alongside a radially polarized HeNe laser at 632.8 nm wavelength, 750 μW of intensity with 0.5 s of accumulation time. Plasmon-tunable tip pyramids (PTTPs)[31] adjusted to the incident laser's wavelength were used for near-field investigations. Following data acquisition, the PortoFlow Analysis Software (v1.16) processed spectral information.

3. CONTINUUM ELASTICITY SIMULATIONS

Continuum elasticity calculations were used to assess the effects of in-plane strain in our graphene layers.[32] Using a commercial finite element model software (COMSOL[33]), each graphene layer was modeled as a homogeneous thin slab characterized by well-defined elastic constants and predefined in-plane strains, an approach that is appropriate for micrometer-sized graphene grains.[34,35] The strain between the layers is treated as homogeneous at the interface for a fixed twist angle, enabling us to accurately capture the average buckling behavior expected from such configurations. These simulations also provide a suitable range of elastic constants for tBG, which are known to differ from monolayer graphene and can be used as a starting point for future works and further developments from other groups.

4. RESULTS

A schematic representation of the twisted bilayer graphene (tBG) lattice exhibiting a moiré pattern due to the mismatch angle between upper and lower graphene sheets is depicted in Figure 1a. Employing atomic force microscopy (AFM), we successfully scanned the surface topography of the tBG, as shown in Figure 1b. Although our tBGs are, in most of their surface area (~95%), characterized by flat regions, buckled structures such as the one shown are commonly observed. The wrinkled structure of Figure 1b has an average height of 60 nm at its center. Since similar morphologies are observed over the tBG surface it is crucial to understand whether local elastic conditions determine the uprising of such features. The particular structure shown here is extensively analyzed throughout this work and its morphology as well as inhomogeneous local strain conditions were observed in other buckled regions in our tBG.

In the same region mentioned above we measured Raman spectra using TERS mapping procedures. Figure 1c displays the Raman spectrum featuring the characteristic Raman bands of a tBG, most notably the R band. As discussed in previous works,[36] the frequency of the rotationally induced R band is associated with a Raman process involving the scattering of a photoexcited electron by a phonon with wavevector q. Momentum conservation is ensured when the electron is elastically scattered by a superlattice wavevector $-q$ determined by the rotational angle θ. Additionally, the stretching motion of the bonds between carbon atoms gives rise to the G band (E_{2g},≈1585 cm^{-1}), while the breathing motion of carbon hexagons correspond to the so-called 2D band (A_{1g}, a second-order feature observed at ≈2650 cm^{-1} for the HeNe laser).

In all the maps presented in this work, each pixel represents an area of 25 × 25 nm^2, with every pixel containing a measured Raman spectrum. The Lorentzian fitting is used to determine the center position of each peak along the frequency axis. Such information is subsequently transcribed into maps that illustrate variations in the intensity and position of each band, providing detailed insights into the localized morphologies and their related electronic properties along the tBG.

Figure 1d shows the variation in the R band peak position (ω_R) within the mapped area. We observe three distinct regions with different mismatch angles, separated by the buckled region (larger wrinkle in the map). Previous studies by Carozo et al.,[36] have established that the R band arises from a double-resonance Raman process involving both elastic and inelastic scattering of electrons mediated by the static potential and phonons, respectively. The process begins with the absorption of a photon of energy E_L and wavevector k_0. The electron then undergoes an elastic scattering event via static potential, which transfers momentum characterized by the rotational wavevector q, scattering the electron to a state with wavevector $k'_{int} = -k_{int}$ on the same energy circle of radius k_{int}. Subsequently, a phonon with wavevector Q_{int} is generated in the lattice, and the electron is inelastically scattered back to k_{int}.

These two events are classified as intervalley or intravalley depending on whether the processes occur between distinct K and K′ Dirac cones (intervalley—the R band) or within the same cone (intravalley−R′ band). Finally, the electron recombines with a hole, emitting a photon with energy $\hbar\omega_S = E_L - \hbar\omega$ (where ω is the phonon frequency) with an additional wavevector k_s. Momentum conservation is satisfied only if the condition $k_0 + k_S = q(\theta) - Q_{int}(\theta)$ is met. Given that the photon k_0 and k_S are small compared to the size of the first Brillouin zone, this condition simplifies to $Q_{int}(\theta) \simeq q(\theta)$.

Our tBG sample was fabricated with a nominal twist angle of 10°. Previous works[37,38] have established the correlation between the dispersion of the acoustic and optical phonons with the twist angle θ and can be used to verify our particular condition. In these works, samples with different twist angles were systematically probed.[27,36,39] We employed here a continuous interpolation of this dispersion as the primary input for phonon frequencies as a function of the rotational angle θ. One must mention here that the experimental (monotonic) R-band frequency (ω_R) shift as a function of twist angle and its consequent theoretical phonon dispersion relation allows us to retrieve a unique correspondence for $\omega_R(\theta)$. Details of this approach are depicted in the Supporting Information, providing the twist angle map shown in Figure 1e. This analysis reveals a variation in the twist angle from 10.8 to 12° across the mapped area as shown. In this figure, three distinct regions are observed, each exhibiting approximately constant angles. Notably, the boundaries between these regions coincide precisely with the location of elongated wrinkles.

The mismatch angle between the graphene layers in tBG plays a crucial role influencing the intensities of both the G and R Raman modes due to resonance effects. In a usual resonant Raman experiment, the photon energy of the laser is tuned to match the energy of electronic signatures such as the van Hove singularities (vHs). For tBG this resonant enhancement is

https://doi.org/10.1021/acs.jpcc.5c00506
J. Phys. Chem. C 2025, 129, 7508−7519

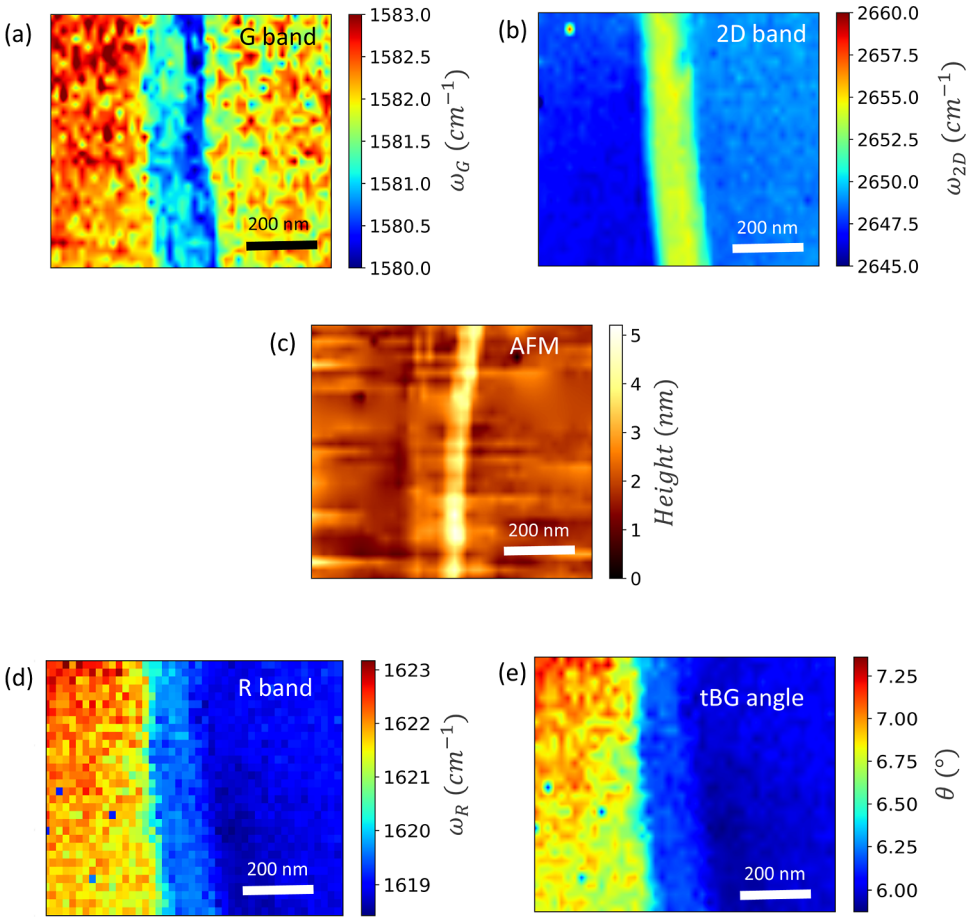

Figure 2. Spatially resolved maps of twisted bilayer graphene obtained using TERS and topography measurements. The maps show variations in (a) G band peak position, (b) 2D band peak position, (c) surface topography, (d) R-band position from the in-plane longitudinal optical (iLO) band and (e) twist angle (θ). The color scales indicate the range of Raman shifts in cm^{-1} for each band, height in nanometers for the topography map and twist degrees for angle distribution, respectively.

particularly sensitive to small changes in the twist angle, as the energy gap between the vHs is highly dependent on the angle.[28,29,40] For instance, we observed that the intensity of the G band decreases by a factor of 2.3 for a 0.8° variation in the twist angle, and by 5.8 for a 1.4° variation (the phenomenon is illustrated in the Supporting Information. A nonuniform distribution of G band intensity across the samples indicates local heterogeneity, requiring detailed investigations to address the variations in angle and strain distributions within the scanned area.

Figure 2 summarizes the results obtained in another sample with a misorientation angle of ∼6°. Hyperspectral analysis focused on the G and 2D bands [Figure 2a,b, respectively] indicates that the prominent changes in these bands' frequencies are restricted to the wrinkled regions. Both 2D and G bands exhibit a shift as they are probed across the nearly vertical line that separates these two regions, suggesting the existence of a physical boundary that divides the tBG into distinct areas. The AFM analysis of this region [Figure 2c] confirms the presence of a wrinkled structure. The TERS spectral image obtained over this $1.0 \times 0.5\ \mu m^2$ area reveals two distinct θ domains within the mapped area. Modifications in the R band were also observed outside the wrinkled areas, confirming the variation in the twist angle as the system moves across a buckled region as shown in Figure 2d. Employing the same analytical procedures as previously used we estimated the local twist angles, mapped out in Figure 2e.

5. DISCUSSION

The data previously exposed show the variation of near-field peak positions of G and 2D bands, that exhibit distinct behavior in the wrinkled region. The G band peak, observed around 1582 cm^{-1}, shows a moderate shift across the wrinkled area, accompanied by a significant, monotonic increase in its full width at half-maximum (fwhm), from 9 to 11.5 cm^{-1}. In contrast, the 2D band peak position consistently shifts toward lower wavenumbers within the wrinkled regions, with the appearance of two distinct peaks, as shown in Figure 3. An analysis of both 2D band peaks was carried out and yielded the following result: the right peak (large wavenumbers) remains stable within the wrinkle, with its fwhm only changing at the wrinkle's edges, exhibiting a monotonic increase from 20 to 60 cm^{-1}. Meanwhile, the left peak (low wavenumbers) shows significant shifts inside the wrinkle. Details are depicted in the Supporting Information. Additionally, the fwhm of the left peak increases in regions where the wrinkle morphology gets higher. This behavior indicates that the 2D band is sensitive to local buckling formation processes in the tBG system.

To directly investigate the behavior of the 2D band along the buckled area shown in Figure 1b and in flat regions of tBG, individual Raman spectra along the linear path depicted in this

https://doi.org/10.1021/acs.jpcc.5c00506
J. Phys. Chem. C 2025, 129, 7508−7519

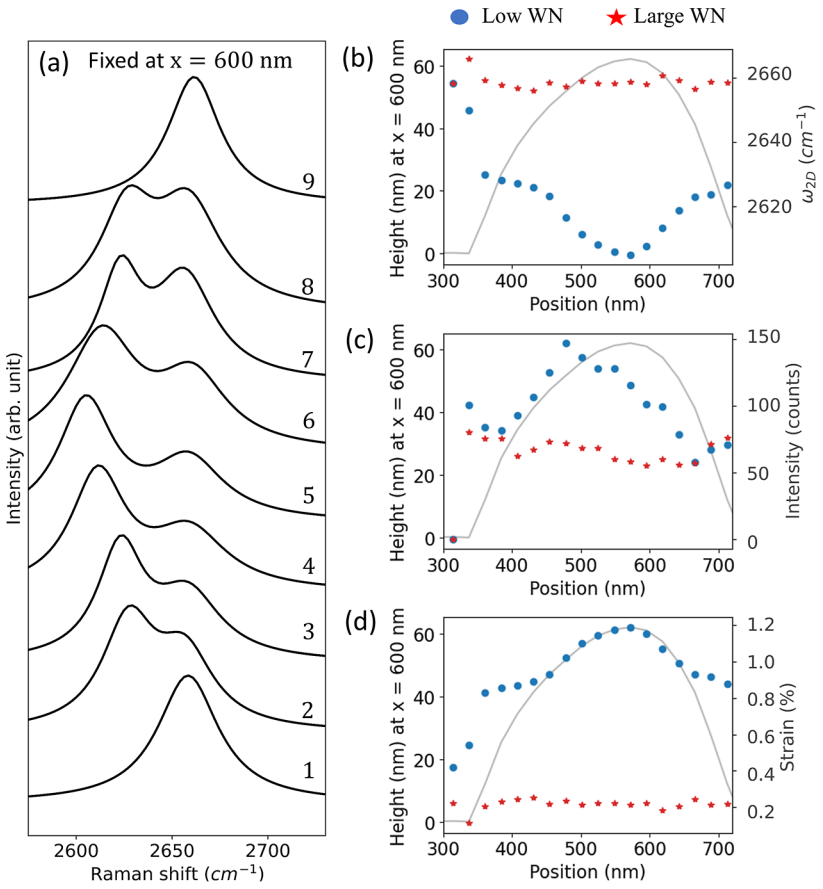

Figure 3. (a) Series of Raman spectra taken at different positions near a wrinkled area, labeled from 1 to 9 and indicated by white dots in Figure 1b. This data set shows the occurrence of two distinct Raman peaks within the buckled areas of the tBG. The variations in peak position, intensity, and strain for each peak are analyzed and depicted in subsequent parts of the figure: (b) shows the peak positions, (c) displays the peak intensities, and (d) presents the calculated strain values, with the lower wavenumber peak represented by blue dots and the large wavenumber peak by red stars. The *x*-axis in panels (b−d) depict the position inside the buckled area along its transversal direction, while the left *y*-axis show the height of the analyzed wrinkle, depicted by the gray solid line, highlighting the structural features of the graphene's deformation.

figure are shown in Figure 3a. All positions marked by white dots in Figure 1b were used to label the explicit spectra from 1 to 9, allowing the spatial correspondence with locations in the TERS map. In this analysis, two distinct behaviors are observed: the emergence of an additional Raman peak at lower wavenumbers inside the wrinkled area, resulting in a superposition of two peaks, and the shift of this additional peak along the labeled path, with the most significant shift occurring at the center of the wrinkle, at its maximum height. One must notice that the peak at lower wavenumbers appears only where wrinkled regions are probed and is more intense than the standard 2D peak observed at flat regions. In flat regions the 2D peak remains unchanged in both position and intensity. Both phenomena are visually represented in Figure 3b,c, where the positions of the left (additional, hereafter referred as lower wavenumber peak) and right (standard 2D peak, referred in the following paragraphs as large wavenumber peak) peaks are indicated by blue dots and red stars, respectively. It is arguably then whether this shift and the presence of the additional peak provide unambiguous strain information about the buckled area. The smooth changes in peak position also suggest the presence of a strain gradient with local variations within the tBG wrinkled structure and adjacent flat layers.

Previous works have used the 2D band Raman shift to estimate the strain level in atomically thin single layer graphene.[41−45] The origin of the 2D band in graphene, as well as in tBG, is associated with double-resonance processes involving the scattering of high-energy phonons near the *K* point of the Brillouin zone. In tBG the superposition and rotation of layers modify the electronic band structure but the fundamental phonon scattering mechanism remains unchanged with respect to that of monolayer graphene. Consequently, the equation should be applicable for estimating strain, although the resulting values may be understood as an upper limit for strain values. Such condition is due to the strain distribution between the two layers, in contrast to the single layer system where it would be fully applied to one graphene sheet. In order to validate this approach, we present at the end of this section finite element modeling calculations that indicate to our approach as a reliable approximation for correlating strain and the Raman shift in twisted bilayer graphene.

It is also known that tBG has built-in strain among layers, that may interfere with in-plane layer accommodation and may induce local buckle-up phenomena (wrinkling) in graphene layers. In such case both layers must accumulate sufficient elastic energy to overcome adhesion forces with the hBN substrate.[46] Using a quantitative inherent strain gauge, provided by changes in the Raman spectrum (see Mohiuddin et al.[41] for details), we directly relate changes in Raman peak positions to the strain induced in the vicinity of wrinkles. The values of the peak position of the 2D band can be then directly used as input for the relation established in ref 41 for in-plane strain

https://doi.org/10.1021/acs.jpcc.5c00506
J. Phys. Chem. C 2025, 129, 7508−7519

$$\Delta\omega_{2D} = -\omega_{2D}^{0}\gamma_{2D}(1-\nu)\epsilon \quad (1)$$

where ω_{2D}^{0} is the expected peak position of the 2D band in the absence of strain, namely 2650 cm^{-1}, γ_{2D} is the Grüneisen parameter for the second order Raman scattering process, and ν = 0.33 is the in-plane Poisson ratio. Additionally, reference Mohiuddin et al.[41] provides the relation $\frac{\partial\omega_{2D}}{\partial\epsilon} \sim -64 cm^{-1}/\%$, used here to calculate the strain for the low wavenumbers and large wavenumber peaks, providing the result depicted in Figure 3d.

To illustrate analytically the largest possible deviations of the results obtained, we consider two systems: (i) a single layer graphene with a lattice parameter a_f is deposited on an infinite substrate with a similar lattice parameter a_s. In such configuration the host substrate is too rigid and will not deform by the presence of the one-atom-thick graphene. Considering a lattice registry between graphene and substrate, any applied strain ($\varepsilon_{\parallel}$) can be then determined using the relative difference between a_f and a_s ($\varepsilon_{\parallel} = [a_f - a_s]/a_s$). In the opposite (and realistic) case (ii), a finite substrate with the same thickness and elastic modulus of the single layer graphene (the second layer in the tBG) shares the strain imposed on the first layer. Since in this configuration any strain caused in the upper layer a_u affects is shared with the lower layer a_l the strain must be computed using the average lattice as the reference value, leading to a modified relationship between the strain and lattice parameters: $\varepsilon_{\parallel} = 2[a_u - a_l]/[a_u + a_l]$ (see Supporting Information). For large strain values, such as $\varepsilon_{\parallel} = 0.2$, the difference between the infinite and finite substrate models results in an error of approximately 10% in strain determination. Conversely, for smaller strain values, around $\varepsilon_{\parallel} = 0.01$, which are the focus of this study, the error is significantly reduced to approximately 1%.

The strain calculated for the 2D large wavenumber peak is approximately constant inside the buckled area, with an average value of 0.4%, as indicated by the red stars in Figure 3d. On the other hand, the strain calculated using the 2D low wavenumber peak varies, exhibiting a trend that follows the height profile, as shown by the blue dots in Figure 3d. We must emphasize that the strain value for the low wavenumber peak (around 0.2%) is always larger than the strain calculated using the large wavenumber peak, ranging from 0.85% at the edge to 1.15% at the top of the wrinkle, similar results were found in other samples as depicted in Supporting Information.

Further support to the strain modeling is provided analyzing the relationship between the 2D and G band frequencies. By plotting the frequencies of these bands and performing a linear fit, we identified three distinct regions, all presenting the same angular coefficient of 2.2, as shown in Figure 4a. The spatial location of each of these regions is depicted in Figure 4b. The slope analysis used here to identify strain and doping in graphene was introduced in reference Lee et al.[47] and successfully applied for analysis in tBG in previous works.[16] Lee observed that the relationship between ω_{2D} and ω_G remains linear but exhibits distinct slopes depending on graphene conditions, with values of 2.2 for strain (isodoping), 0.75 for p-type doping.

Since 2D band splits into two peaks inside the wrinkled region, each exhibiting details of one type of strain, we can plot them separately to find the spatial distribution in the mapped region. Figure 5a shows the regions where the 2D band has one peak (black regions) and where it has two peaks (white regions). Figure 5b displays the relative intensity between the low

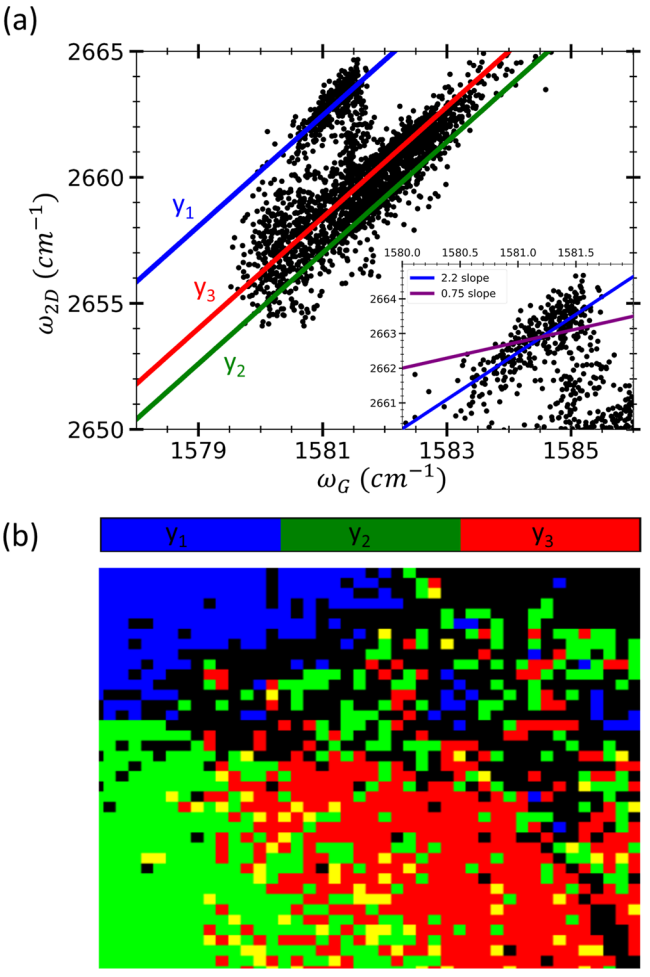

Figure 4. (a) The ratio between the peak positions of the 2D and G bands. Linear regressions were carried out on data points, highlighting three distinct behaviors represented by the different colors. (b) A reconstructed map based on the points highlighted on the linear regression. The color code used in the regression corresponds to the domain colors in the spatial map.

wavenumber peak, I_{Lowwn}, (in regions with two peaks) and the large wavenumber peak intensity, $I_{Largewn}$, (in regions with one peak and/or where large wavenumber peak appears in regions with two 2D band peaks). The intensity of the low wavenumber peak is consistently higher than that of the large wavenumber peak (where both coexist), with the most significant intensity contrast observed around the wrinkle's center. This indicates that the wrinkle formation is related to in-plane strain conditions that require the coexistence of biaxial and uniaxial strain contributions.

In general, compressive strain results in an upshift of all Raman peaks, arising from the shortening of the interatomic bond lengths, while tensile causes a downshift, due to the elongation of the bond lengths resulting in a weakening of the vibrational modes. Biaxial strain preserves the hexagonal symmetry in single layer graphene, leading to an isotropic expansion or compression of the hexagonal lattice, resulting in a linear peak shift. Uniaxial strain also results in linear peak shifts but result in breaking the hexagonal symmetry, which has an effect on the Raman peak shape.[48] The splitting of the 2D peak discussed previously has been reported whenever the uniaxial strain exceeds ~0.5% and is applied along a high-symmetry axis.[42−44,48] In the graphene structure, each K point has three

https://doi.org/10.1021/acs.jpcc.5c00506
J. Phys. Chem. C 2025, 129, 7508−7519

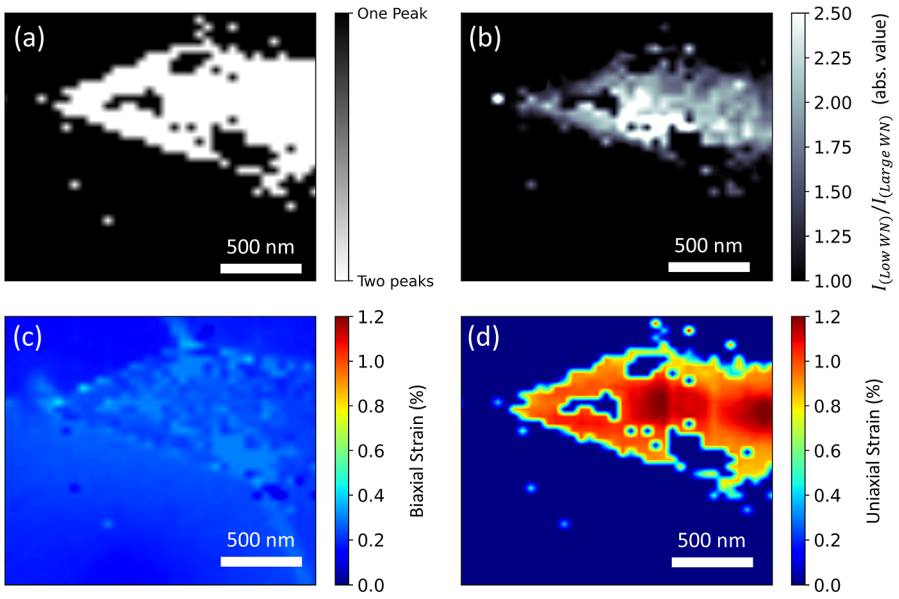

Figure 5. : (a) Binary map of regions where the 2D band exhibits one peak (black) and regions where it shows two peaks (white). (b) Grayscale map showing the relative intensity of the low wavenumber peak compared to the large wavenumber peak. (c) Map of the calculated biaxial strain for regions with a single 2D peak and/or the low wavenumber 2D peak where two peaks are present. (d) Map of the calculated uniaxial strain using the large wavenumber 2D peak in regions where two peaks are observed.

neighboring K' points, leading to three contributions to the scattering process. The relative position of the Dirac points is therefore disturbed under uniaxial strain, implying that the three scattering mechanisms connecting $\boldsymbol{K}$ and $\boldsymbol{K}'$ are no longer identical.[42,43,48] The most probable condition for the uniaxial strain scenario of wrinkles imply that two of the three possible scattering mechanisms lead to one 2D peak component, while the remaining (uniaxially strained) one gives rise to the second 2D peak component. This scenario is more complex at a grain boundary, depending on if the direction of the strain is parallel or perpendicular to an armchair edge in graphene.

Besides the presence of uniaxial strain, the observation of biaxial strain is associated with the peak center shift in regions with a single peak. The large wavenumber peak is still related to biaxial strain in regions where two 2D peaks are present. This allows us to calculate the biaxial strain using eq 1. Figure 5c shows the map of the calculated biaxial strain, indicating values ranging from 0.2% to 0.4% both within and outside the wrinkled area. It is evident that the biaxial strain is almost uniform in these regions, suggesting it is induced by the layer twist and not modified upon buckling.

In contrast with isotropic in-plane biaxial strain, local fluctuations in graphene can lead to deviations that result in a predominance of uniaxial strain, typically observed at the crests of wrinkles. Leveraging the findings from Yoon et al.[43] where controlled mapping of applied strain results in 2D band splitting, we further explore this phenomenon. Consistently with previous studies (e.g., refs 38, 39 and 40), simultaneous shift in the Raman modes and the 2D band splitting are retrieved when strain is externally applied. Both phenomena are used, often together, to quantify the strain load on the sample. The peak at low wavenumbers, associated with uniaxial strain, is analyzed to provide in Figure 5d a map of uniaxial strain, highlighting remarkable differences from pure biaxial strain scenarios. The uniaxial strain values, found to range from 0.85% to 1.15%, are approximately 4 times higher than the biaxial strain values. The highest uniaxial strain values are located in areas where the graphene is significantly buckled, corresponding to large values of layer height. This evidence suggests that uniaxial strain plays a crucial role in the formation of buckling in these areas, requiring the use of strain simulations to corroborate such interpretation (see the following paragraphs). The analytical approach described here can indeed be extended to estimate the strain across the entire mapped area by considering both biaxial and uniaxial strains. In Figure 6a the total in-plane strain values across the sample are shown.

Further analysis can be carried out evaluating the strain field evolution by calculating the Laplacian of the in-plane strain data. The resulting map, displayed in Figure 6b, highlights areas with the most pronounced lattice changes. These regions are predominantly retrieved at the borders of wrinkles, where the onset of buckling-induced changes in elastic energy is observed. To directly quantify this phenomenon, the elastic energy of the system is quantitatively evaluated, providing a comprehensive understanding of the mechanical stresses and their distribution within the tBG system. The elastic energy U stored inside any strained structure with a hexagonal lattice system can be estimated as

$$U = \left(C_{11} + C_{12} - \frac{C_{13}}{C_{33}}\right)^2 \varepsilon^2 \tag{2}$$

where C_{11}, C_{12}, C_{13} and C_{33} are the elastic constants of the graphene stress−strain tensor. The values for these coefficients were estimated in previous works,[49] in which 1109, 275, 0.59, and 36.5 GPa, were ascribed to C_{11}, C_{12}, C_{13} and C_{33}, respectively. An elastic energy map is shown in Figure 6c. Our calculations using experimental Raman data in the wrinkled regions retrieved values up to 12 meV/atom, indicating that buckling stability may be overcome at mild annealing temperatures near 700 K. This temperature is roughly two times the elastic energy stored in two graphene unit cells (96 meV, accounting for the upper and lower sheets) in a wrinkled region and may remove the system from local energy minima achieved

https://doi.org/10.1021/acs.jpcc.5c00506
J. Phys. Chem. C 2025, 129, 7508−7519

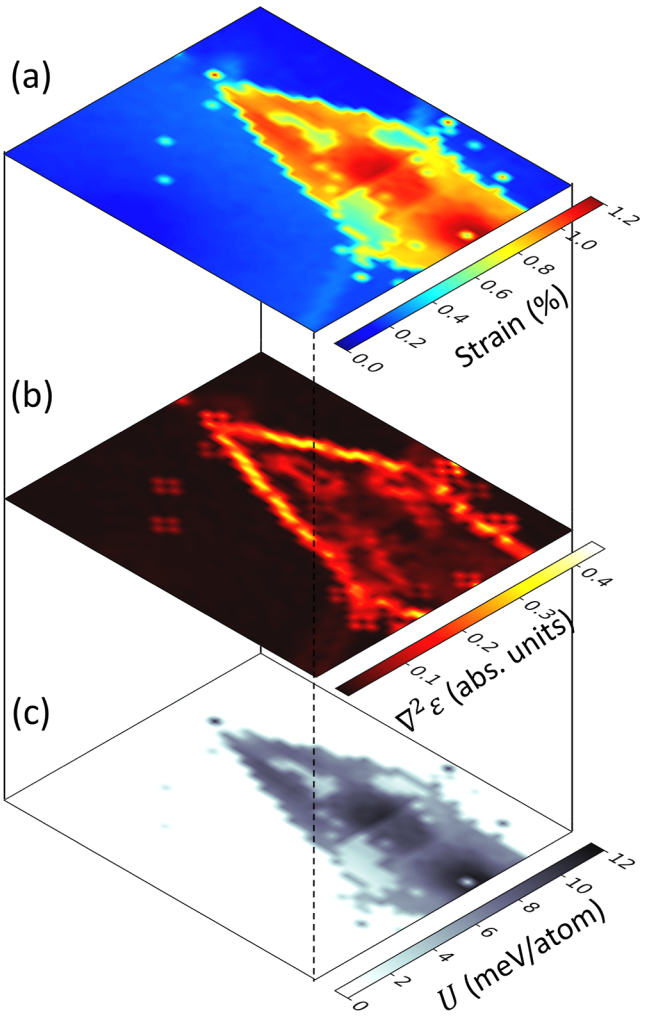

Figure 6. (a) Total in-plane strain mapping obtained from hyperspectral analyses correlating the peak positions of the 2D band. (b) In-plane Laplacian of the strain map, highlighting the more pronounced strain changes surrounding wrinkled areas. (c) Elastic energy in meV/atom calculated for a hexagonal lattice system.

upon tBG buckling. Further research is necessary to assess the evolution of strain in graphene bilayers within this temperature range, where thermal dynamics can become crucial for modifying the buckling distribution in the twisted bilayer graphene (tBG) system prior to device fabrication.

At this point one may argue about possible variations between single layer graphene and tBG elastic constants and the possibility to simulate wrinkles in this system. Previous works from our group[34,35] have dealt with rolling-up graphene in large areas under controlled conditions, achieving radii down to 500 nm.[35] These experiments were performed in 1, 2, and 3 stacked graphene layers. The most remarkable changes take place from 1 graphene layer, where $E = 800 \pm 30$ GPa was retrieved, to 2 graphene layers, where $E = 700 \pm 40$ GPa was found (a similar value was found for 3 graphene layers). In all cases the in-plane Poisson ratio remains the same: $\nu = 0.20 \pm 0.02$. Since large area CVD graphene sheets were used no specific crystalline registry was observed among stacked graphene layers. We therefore assume in the following continuum elastic simulations that 800 GPa is the upper limit for tBG Young Modulus, while the multilayer graphene Young modulus represents a lower limit. Since the corroboration of strain anisotropy scenario is crucial for buckling investigation, we fixed $E_{tBG} = 750$ GPa along the following calculations. This implies in a conservative error estimation of ~6% for our findings.

To deepen our understanding of wrinkle formation triggered by nonuniform strain, we developed a simplified finite element model (FEM). This model approach is particularly beneficial for examining the effects of strain inhomogeneity under realistic conditions, providing a clearer picture of how these factors influence material behavior at the nanoscale. A slice of 10° of a circle with a 2.5 μm radius was created, and the anisotropic single layer graphene elastic constants from Bosak et al.[49] were introduced with a modification of ~6% in values in order to yield $E_{tBG} = 750$ GPa (as discussed above). These constants were then set into two continuous graphene sheets with a thickness of 1.5 Å each. One of the in-plane axes for the lower graphene layer was aligned with a crystal in-plane direction (a or b in the unit cell) to facilitate result interpretation. Although the layer thickness may indicate the need to use atomistic models in the out-of-plane direction, graphene sheets can be approximated by continuous elasticity systems along the in-plane direction whenever the crystalline grain size is larger than a few microns (see, e.g., refs 34 and 35).

In our finite element model (FEM) simulations, we introduced several combinations of strain values ranging from 0 to 1.5% between the graphene sheets at the outer and inner areas of the slice. The boundary condition for the outermost part of the bilayer graphene slice, positioned 2.5 μm from the center of the wrinkle, was set as fixed (the outer rim cannot be displaced). This condition represents a finite distance for strain relaxation in the flat areas of graphene. To replicate the 60 nm wrinkle height observed in the AFM data of Figure 1b, we set the biaxial strain at 0.25% in the outer regions of the simulated bilayer.

In the inner regions, a larger strain value was necessary to achieve the observed wrinkle height and to align with the expected Raman strain distribution. This was accomplished by imposing a 1.15% uniaxial strain. It is important to note that in the FEM simulation, achieving higher buckling configurations in the inner region required adjusting the strain values due to the lattice symmetry and the anisotropic elastic properties of graphene. Specifically, the radial strain (along the slice's lateral axis) was kept at 0.25%, while the tangential in-plane strain was set at 1.15%.

This configuration demonstrates that wrinkling can effectively relax strain along its transversal axis. Additionally, our results indicate that such buckling does not modify the system condition below the original 0.25% biaxial strain caused by the bilayer twist, which remains unchanged in the wrinkled area. The elastic energy observed in the FEM simulations for the graphene wrinkles was found to be in the range of 8−11 meV/atom, corroborating the experimental findings presented in the lower panel of Figure 7a. This alignment between simulation and experimental data highlights the effectiveness of our model in capturing the complex mechanical behavior of strained bilayer graphene. The results also imply that $E_{tBG} = 750 \pm 50$ GPa is a reliable approximation in this system.

The deviation noted in the solid blue line fit in Figure 7b, comparing simulated and AFM height profiles at the wrinkle's base, is attributed to the simplified, abrupt transition used in the FEM model between the in-plane outer and inner regions. Implementing a smoother transition in the model, which would account for gradual changes in uniaxial strain across these regions requires a larger set of variables which may need changes

https://doi.org/10.1021/acs.jpcc.5c00506
J. Phys. Chem. C 2025, 129, 7508−7519

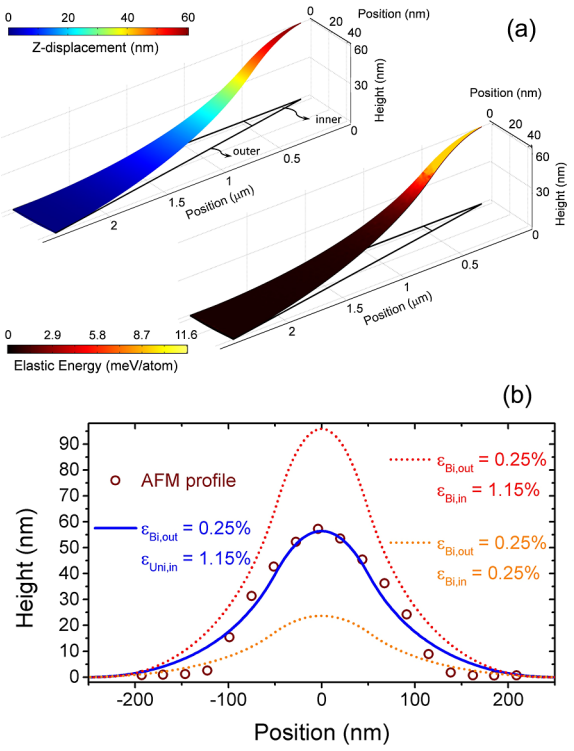

Figure 7. (a) FEM simulation result of strain and elastic energy for a graphene bilayer with a constant 0.25% in-plane biaxial strain in the outer region (see figure) and additional 1.15% uniaxial in-plane strain in the inner region. The simulation has cylindrical symmetry in the graphene layer plane. (b) Superposition of FEM simulations (lines) and AFM data (dots) for a wrinkle with 250 nm lateral base size measured by AFM. The solid line represents the best fit with biaxial strain in the outer region and a pronounced uniaxial strain in the inner region (see text for details). Dashed lines accounting distinct proportions of uniaxial and biaxial strain are also displayed for clarity.

depending on wrinkle crystallographic orientation, losing its broad character.

In Figure 8, we illustrate the close agreement between the finite element model (FEM) simulation, which incorporates 0.25% biaxial strain in the outer region and 1.15% uniaxial strain in the inner region (expressed in terms of its quantitative difference to the biaxial strain), and the atomic force microscopy (AFM) data derived from Figure 1b, as well as other buckled regions of the sample. It becomes then possible to assess whether the strain interpretations accurately reflect the behavior across wrinkles with varying heights. To explore this, we adjusted the radius of the inner region in our finite element model (FEM) from 10 to 500 nm, in increments of 10 steps, effectively altering the diameter of the buckled area from 20 to 1000 nm. We then varied the uniaxial strain along the tangential direction in increments of 0.05%, maintaining a constant 0.25% biaxial strain in the outer region and a 0.25% radial strain in the inner region. In all scenarios, an upward buckling of the bilayer was induced (as opposed to downward buckling, which occurs under negative or tensile strain values). The resulting data on the maximum height of the buckled FEM layers established upper and lower boundaries for the differences between uniaxial and biaxial in-plane strains, set at 0.70% and 0.95% (represented by blue and pink dashed lines, respectively). These specific values were selected to establish practical lower and upper bounds for the uniaxial tangential strain, corresponding to uniaxial strains of 0.95% to 1.20%, respectively.

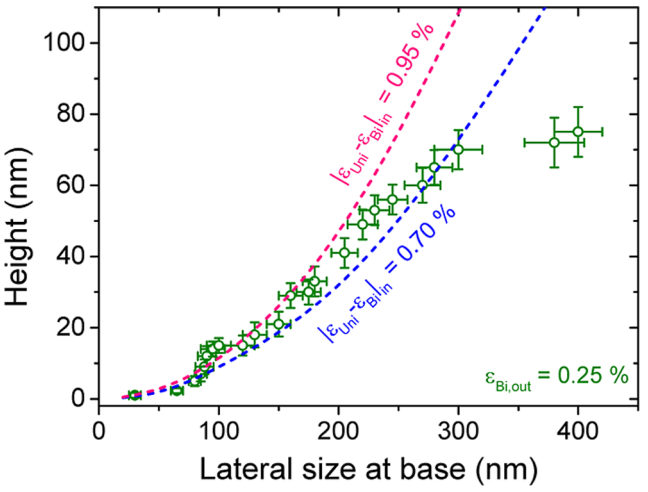

Figure 8. Plot of wrinkle height AFM measurements (dots) as a function of wrinkle lateral size at the base for distinct wrinkles regions in our sample. Dashed lines represent expected continuum elasticity behavior simulated using FEM for two distinct anisotropic strain values for larger tangential uniaxial strain relatively to the local biaxial values: 0.70% (blue line) and 0.95% (pink line). In all cases a biaxial strain of 0.25% was set at the outer FEM simulated region, with a similar value holding for the inner region strain along the radial direction.

In most instances, particularly for wrinkles with a lateral base size exceeding 100 nm, a tangential uniaxial strain that is 0.85% larger than the biaxial strain predominates in this configuration of twisted bilayer graphene (tBG). However, distinct in-plane strain conditions are observed for wrinkles with reduced heights (below 15 nm) and smaller lateral sizes (below 100 nm). For larger lateral sizes, exceeding 300 nm, a threshold wrinkle height of approximately 75 nm is consistently observed in the studied area. Notably, no heights above this threshold were recorded experimentally in our sample, suggesting that both in-plane boundary conditions and inhomogeneities in the bilayer van der Waals interactions contribute to stabilizing the height of the resulting structures. These inhomogeneities at the atomic level likely induce the local maximum absolute 1.15% in-plane strain, which is then anisotropically released during wrinkle formation.

By reproducing this data set our model shows its ability to replicate in a simple form the wrinkle formation observed in twisted bilayer graphene (tBG). Additional simulations that employed purely biaxial strain across both regions failed to replicate the wrinkle height cross-section with parameters like those obtained from tip-enhanced Raman scattering (TERS) measurements.

This comparative analysis demonstrates that our FEM model effectively captures the essential characteristics of strain-induced wrinkle formation in tBG, offering valuable insights into the dynamics of biaxial and quasi-uniaxial strains. These insights are crucial for understanding how different strain configurations influence the topographical features of tBG, enhancing our ability to predict and manipulate these structures in practical applications. FEM simulations highlight the critical role of uniaxial in-plane strain and boundary conditions in both the formation and stability of wrinkled regions, thereby enhancing our understanding of strain-induced phenomena in twisted bilayer graphene. This knowledge is vital for predicting and controlling the mechanical stability and electronic properties of tBG, which is key for the development of advanced graphene-based technologies.

https://doi.org/10.1021/acs.jpcc.5c00506
J. Phys. Chem. C 2025, 129, 7508−7519

Finally, there is an increasing interest in low twist tBG configurations since it leads to desired changes in electronic structure and does not induce strong wrinkling phenomenon as discussed in our work. A general qualitative scenario for wrinkling/buckling occurrence can be described as follows. Elastic and plastic relaxation have an interplay in graphene systems that strongly depend on domain (grain) size. Grain boundaries can deform the lattice without following continuum elasticity processes, that are at the origin of wrinkling phenomena. If the system is subjected to a reduced twist angle, and consequently a small in-plane strain, it may happen that the expected elastic relaxation takes place at the grain boundaries and no buckling is observed (for micrometer-sized single-crystalline regions). On the other hand, if large twist angles are induced, impling in in-plane strain conditions where sufficient elastic energy is stored for a reduced graphene layer area. Such condition will drive the system into the generation of morphological features (wrinkles, buckled regions) that locally affects the spatial strain distribution. As the in-plane strain increases, one expects to observe a larger density of wrinkled regions. Therefore, such interplays of domain size and twist angle/strain must be taken into consideration in order to minimize or suppress buckling in tBG systems.

6. CONCLUSION

In summary, our study demonstrates that the mismatch angle in the bilayer graphene can induce strain conditions with enough stored elastic energy to generate localized strain gradients, leading to the formation of buckled regions. We quantified local strain variations using tip-enhanced Raman spectroscopy (TERS), which enabled the evaluation of Raman peak shifts on a nanometric scale. Notably, the emergence of a new peak within the wrinkled regions allowed us to distinguish between uniaxial and biaxial strain influences, providing an evidence of anisotropic strain conditions in these features.

Our findings indicate that uniaxial strain plays a pivotal role in the formation of wrinkles. Through detailed analysis of the strain and its gradients, we were able to estimate the elastic energy involved, providing experimental evidence of the energies that drive the wrinkling processes within this system. To further understand the topographical changes associated with these strain conditions, we developed a finite element model (FEM) that incorporates nonuniform strain and its consequences to the observed morphologies. This model showed good agreement with our experimental observations and was able to capture the most relevant aspects of wrinkles in tBG, such as wrinkle height and stored elastic energy. The findings support the condition of anisotropic, strong uniaxial in-plane strain as the primary driving force behind wrinkle formation, under conditions where wrinkle radial strain is relaxed while a larger tangential strain persists at the borders of buckled regions.

These conditions manifest as nanoscale features in tBG flakes, with wrinkle heights ranging from 5 to 80 nm and wrinkle-to-wrinkle separations larger than hundreds of nanometers, indicating that wrinkling is a mechanism for overall graphene sheet accommodation. Our research enhances the understanding of mechanical and structural dynamics in tBG, providing valuable insights that could lead to the development of strategies for engineering graphene-based materials with tailored properties, including thermal treatments in tBG after deposition for minimization of buckling effects.

Besides the expected electronic modifications that take place due to the twist angle in tBG systems, changes of surface chemical activity may also take place. The spatial distribution of biaxial and uniaxial strain and the consequent variations in local electronic density and elastic energy are sufficiently strong to generate preferential sites for adsorption of molecules, nucleation and clustering of adatoms upon deposition and enhancement/reduction of local chemical selectivity. Such conditions vary according to the density of wrinkles and the stored elastic energy and strain imposed by the twist angle, and play the role of an additional degree of freedom for surface chemical activity. They are able to potentialize the use of tBG for tuning the performance of devices that depend on electrochemical response such as sensors.

■ ASSOCIATED CONTENT

Supporting Information

The Supporting Information is available free of charge at https://pubs.acs.org/doi/10.1021/acs.jpcc.5c00506.

Phonon dispersion/twist angle relationship graphics and maps; additional G band intensity map for the wrinkled region explored in the manuscript; spatially resolved maps of G and 2D bands peak position and width near the large wrinkled region explored in the manuscript; Raman spectral analysis for two additional wrinkled regions; a graphical representation of the continuum elasticity model used in this work (PDF)

■ AUTHOR INFORMATION

Corresponding Author

Angelo Malachias − *Physics Department, Federal University of Minas Gerais, Belo Horizonte, Minas Gerais 31270-901, Brazil;* orcid.org/0000-0002-8703-4283; Email: angelomalachias@gmail.com

Authors

Gustavo Soares − *Physics Department, Federal University of Minas Gerais, Belo Horizonte, Minas Gerais 31270-901, Brazil;* orcid.org/0000-0001-9121-3914

Rafael R. Barreto − *Physics Department, Federal University of Minas Gerais, Belo Horizonte, Minas Gerais 31270-901, Brazil;* orcid.org/0000-0002-4658-5855

Rafael Nadas − *Physics Department, Federal University of Minas Gerais, Belo Horizonte, Minas Gerais 31270-901, Brazil; FabNS, Belo Horizonte, Minas Gerais 31310-260, Brazil;* orcid.org/0000-0001-6165-5981

Kenji Watanabe − *National Institute for Materials Science, Tsukuba, Ibaraki 305-0047, Japan;* orcid.org/0000-0003-3701-8119

Takashi Taniguchi − *National Institute for Materials Science, Tsukuba, Ibaraki 305-0047, Japan;* orcid.org/0000-0002-1467-3105

Leonardo C. Campos − *Physics Department, Federal University of Minas Gerais, Belo Horizonte, Minas Gerais 31270-901, Brazil;* orcid.org/0000-0001-6792-7554

Luiz G. Cançado − *Physics Department, Federal University of Minas Gerais, Belo Horizonte, Minas Gerais 31270-901, Brazil;* orcid.org/0000-0003-0816-0888

Complete contact information is available at: https://pubs.acs.org/10.1021/acs.jpcc.5c00506

Funding

The Article Processing Charge for the publication of this research was funded by the Coordenacao de Aperfeicoamento

de Pessoal de Nivel Superior (CAPES), Brazil (ROR identifier: 00x0ma614).

Notes

The authors declare no competing financial interest.

■ ACKNOWLEDGMENTS

This work was supported by CNPq, CAPES, INCT of Nanocarbono, and FAPEMIG. The authors are thankful to the UFMG Facilities: LabNS, LCPNano and LabNano. G.S.N.E.

■ REFERENCES

(1) Cao, Y.; Fatemi, V.; Demir, A.; Fang, S.; Tomarken, S. L.; Luo, J. Y.; Sanchez-Yamagishi, J. D.; Watanabe, K.; Taniguchi, T.; Kaxiras, E.; et al. Correlated Insulator Behaviour at Half-Filling in Magic-Angle Graphene Superlattices. *Nature* **2018**, *556* (7699), 80−84.

(2) Nuckolls, K. P.; Oh, M.; Wong, D.; Lian, B.; Watanabe, K.; Taniguchi, T.; Bernevig, B. A.; Yazdani, A. Strongly Correlated Chern Insulators in Magic-Angle Twisted Bilayer Graphene. *Nature* **2020**, *588* (7839), 610−615.

(3) Rai, G.; Crippa, L.; Călugăru, D.; Hu, H.; Paoletti, F.; de' Medici, L.; Georges, A.; Bernevig, B. A.; Valentí, R.; Sangiovanni, G.; et al. Dynamical Correlations and Order in Magic-Angle Twisted Bilayer Graphene. *Phys. Rev. X* **2024**, *14* (3), 031045.

(4) Sánchez Sánchez, M.; Stauber, T. Correlated Phases and Topological Phase Transition in Twisted Bilayer Graphene at One Quantum of Magnetic Flux. *Phys. Rev. B* **2024**, *109* (19), 195167.

(5) Choi, Y.; Kim, H.; Peng, Y.; Thomson, A.; Lewandowski, C.; Polski, R.; Zhang, Y.; Arora, H. S.; Watanabe, K.; Taniguchi, T.; et al. Correlation-Driven Topological Phases in Magic-Angle Twisted Bilayer Graphene. *Nature* **2021**, *589* (7843), 536−554.

(6) Gargiulo, F.; Yazyev, O. V. Structural and Electronic Transformation in Low-Angle Twisted Bilayer Graphene. *2D Mater.* **2018**, *5* (1), 015019.

(7) Deng, S.; Cai, X.; Zhang, Y.; Li, L. Enhanced Thermoelectric Performance of Twisted Bilayer Graphene Nanoribbons Junction. *Carbon* **2019**, *145*, 622−628.

(8) Mahapatra, P. S.; Ghawri, B.; Garg, M.; Mandal, S.; Watanabe, K.; Taniguchi, T.; Jain, M.; Mukerjee, S.; Ghosh, A. Misorientation-Controlled Cross-Plane Thermoelectricity in Twisted Bilayer Graphene. *Phys. Rev. Lett.* **2020**, *125* (22), 226802.

(9) Kommini, A.; Aksamija, Z. Very High Thermoelectric Power Factor near Magic Angle in Twisted Bilayer Graphene. *2D Mater.* **2021**, *8* (4), 045022.

(10) Kubakaddi, S. S. Giant Thermopower and Power Factor in Magic Angle Twisted Bilayer Graphene at Low Temperature. *J. Phys.: Condens. Matter* **2021**, *33* (24), 245704.

(11) Liu, S.; Chen, Y.; Zhang, G.; Liu, Y. Tunable Wrinkle Patterns in Moiré Pattern of Interlayer-Bonding Strained Bilayer Graphene. *Appl. Surf. Sci.* **2024**, *657*, 159792.

(12) Bennett, D.; Larson, D. T.; Sharma, L.; Carr, S.; Kaxiras, E. Twisted Bilayer Graphene Revisited: Minimal Two-Band Model for Low-Energy Bands. *Phys. Rev. B* **2024**, *109* (15), 155422.

(13) Wu, Q.; Qian, J.; Wang, Y.; Xing, L.; Wei, Z.; Gao, X.; Li, Y.; Liu, Z.; Liu, H.; Shu, H.; et al. Waveguide-Integrated Twisted Bilayer Graphene Photodetectors. *Nat. Commun.* **2024**, *15* (1), 3688.

(14) Lau, C. N.; Bockrath, M. W.; Mak, K. F.; Zhang, F. Reproducibility in the Fabrication and Physics of Moiré Materials. *Nature* **2022**, *602* (7895), 41−50.

(15) Díez-Mérida, J.; Díez-Carlón, A.; Yang, S. Y.; Xie, Y. M.; Gao, X. J.; Senior, J.; Watanabe, K.; Taniguchi, T.; Lu, X.; Higginbotham, A. P.; et al. Symmetry-Broken Josephson Junctions and Superconducting Diodes in Magic-Angle Twisted Bilayer Graphene. *Nat. Commun.* **2023**, *14* (1), 2396.

(16) Gadelha, A. C.; Ohlberg, D. A. A.; Santana, F. C.; Eliel, G. S. N.; Lemos, J. S.; Ornelas, V.; Miranda, D.; Nadas, R. B.; Watanabe, K.; Taniguchi, T.; et al. Twisted Bilayer Graphene: A Versatile Fabrication Method and the Detection of Variable Nanometric Strain Caused by Twist-Angle Disorder. *ACS Appl. Nano Mater.* **2021**, *4* (2), 1858−1866.

(17) Anderson, M. S. Locally Enhanced Raman Spectroscopy with an Atomic Force Microscope. *Appl. Phys. Lett.* **2000**, *76* (21), 3130−3132.

(18) Hayazawa, N.; Inouye, Y.; Sekkat, Z.; Kawata, S. Metallized Tip Amplification of Near-Field Raman Scattering. *Opt. Commun.* **2000**, *183* (1−4), 333−336.

(19) Stöckle, R. M.; Suh, Y. D.; Deckert, V.; Zenobi, R. Nanoscale Chemical Analysis by Tip-Enhanced Raman Spectroscopy. *Chem. Phys. Lett.* **2000**, *318* (1−3), 131−136.

(20) Sun, M.; Zhang, Z.; Zheng, H.; Xu, H. In-Situ Plasmon-Driven Chemical Reactions Revealed by High Vacuum Tip-Enhanced Raman Spectroscopy. *Sci. Rep.* **2012**, *2* (1), 647.

(21) Domke, K. F.; Zhang, D.; Pettinger, B. Tip-Enhanced Raman Spectra of Picomole Quantities of DNA Nucleobases at Au(111). *J. Am. Chem. Soc.* **2007**, *129* (21), 6708−6709.

(22) Smithe, K. K. H.; Krayev, A. V.; Bailey, C. S.; Lee, H. R.; Yalon, E.; Aslan, B.; Muñoz Rojo, M.; Krylyuk, S.; Taheri, P.; Davydov, A. V.; et al. Nanoscale Heterogeneities in Monolayer $MoSe_2$ Revealed by Correlated Scanning Probe Microscopy and Tip-Enhanced Raman Spectroscopy. *ACS Appl. Nano Mater.* **2018**, *1* (2), 572−579.

(23) Jorio, A.; Saito, R.; Dresselhaus, M. S.; Dresselhaus, G. *Raman Spectroscopy in Graphene Related Systems*; John Wiley & Sons, 2011.

(24) Li, G.; Luican, A.; Lopes dos Santos, J. M. B.; Castro Neto, A. H.; Reina, A.; Kong, J.; Andrei, E. Y. Observation of Van Hove Singularities in Twisted Graphene Layers. *Nat. Phys.* **2010**, *6* (2), 109−113.

(25) Suárez Morell, E.; Correa, J. D.; Vargas, P.; Pacheco, M.; Barticevic, Z. Flat Bands in Slightly Twisted Bilayer Graphene: Tight-Binding Calculations. *Phys. Rev. B: Condens. Matter Mater. Phys.* **2010**, *82* (12), 121407.

(26) Ribeiro, H. B.; Sato, K.; Eliel, G. S. N.; de Souza, E. A. T.; Lu, C.-C.; Chiu, P.-W.; Saito, R.; Pimenta, M. A. Origin of van Hove Singularities in Twisted Bilayer Graphene. *Carbon* **2015**, *90*, 138−145.

(27) Campos-Delgado, J.; Cançado, L. G.; Achete, C. A.; Jorio, A.; Raskin, J.-P. Raman Scattering Study of the Phonon Dispersion in Twisted Bilayer Graphene. *Nano Res.* **2013**, *6*, 269−274.

(28) Carozo, V.; Almeida, C. M.; Fragneaud, B.; Bedê, P. M.; Moutinho, M. V. O.; Ribeiro-Soares, J.; Andrade, N. F.; Souza Filho, A. G.; Matos, M. J. S.; Wang, B.; et al. Resonance Effects on the Raman Spectra of Graphene Superlattices. *Phys. Rev. B: Condens. Matter Mater. Phys.* **2013**, *88* (8), 085401.

(29) Righi, A.; Venezuela, P.; Chacham, H.; Costa, S. D.; Fantini, C.; Ruoff, R. S.; Colombo, L.; Bacsa, W. S.; Pimenta, M. A. Resonance Raman Spectroscopy in Twisted Bilayer Graphene. *Solid State Commun.* **2013**, *175*, 13−17.

(30) Jorio, A.; Cançado, L. G. Raman Spectroscopy of Twisted Bilayer Graphene. *Solid State Commun.* **2013**, *175*, 3−12.

(31) Vasconcelos, T. L.; Archanjo, B. S.; Oliveira, B. S.; Valaski, R.; Cordeiro, R. C.; Medeiros, H. G.; Rabelo, C.; Ribeiro, A.; Ercius, P.; Achete, C. A.; et al. Plasmon-Tunable Tip Pyramids: Monopole Nanoantennas for Near-Field Scanning Optical Microscopy. *Adv. Opt. Mater.* **2018**, *6* (20), 1800528.

(32) Chou, P. C.; Pagano, N. J. *Elasticity: Tensor, Dyadic, and Engineering Approaches*; Dover Publications: New York, 1992; p 53.

(33) *COMSOL Multiphysics v. 3.5*; COMSOL AB: Stockholm, Sweden, 2025. Www.Comsol.Com, https://www.comsol.com/, accessed: 2025−04−03.

(34) Barcelos, I. D.; Moura, L. G.; Lacerda, R. G.; Malachias, A. Observation of Strain-Free Rolled-Up CVD Graphene Single Layers: Toward Unstrained Heterostructures. *Nano Lett.* **2014**, *14* (7), 3919−3924.

(35) Barcelos, I. D.; Marçal, L. A. B.; Deneke, Ch.; Moura, L. G.; Lacerda, R. G.; Malachias, A. Direct Evaluation of CVD Multilayer Graphene Elastic Properties. *RSC Adv.* **2016**, *6* (105), 103707−103713.

(36) Carozo, V.; Almeida, C. M.; Ferreira, E. H. M.; Cançado, L. G.; Achete, C. A.; Jorio, A. Raman Signature of Graphene Superlattices. *Nano Lett.* **2011**, *11* (11), 4527−4534.

(37) Venezuela, P.; Lazzeri, M.; Mauri, F. Theory of Double-Resonant Raman Spectra in Graphene: Intensity and Line Shape of Defect-Induced and Two-Phonon Bands. *Phys. Rev. B: Condens. Matter Mater. Phys.* **2011**, *84* (3), 035433.
(38) Lui, C. H.; Malard, L. M.; Kim, S.; Lantz, G.; Laverge, F. E.; Saito, R.; Heinz, T. F. Observation of Layer-Breathing Mode Vibrations in Few-Layer Graphene through Combination Raman Scattering. *Nano Lett.* **2012**, *12* (11), 5539−5544.
(39) Righi, A.; Costa, S. D.; Chacham, H.; Fantini, C.; Venezuela, P.; Magnuson, C.; Colombo, L.; Bacsa, W. S.; Ruoff, R. S.; Pimenta, M. A. Graphene Moiré Patterns Observed by Umklapp Double-Resonance Raman Scattering. *Phys. Rev. B: Condens. Matter Mater. Phys.* **2011**, *84* (24), 241409.
(40) Campos-Delgado, J.; Cançado, L. G.; Achete, C. A.; Jorio, A.; Raskin, J.-P. Raman Scattering Study of the Phonon Dispersion in Twisted Bilayer Graphene. *Nano Res.* **2013**, *6*, 269−274.
(41) Mohiuddin, T. M. G.; Lombardo, A.; Nair, R. R.; Bonetti, A.; Savini, G.; Jalil, R.; Bonini, N.; Basko, D. M.; Galiotis, C.; Marzari, N.; et al. Uniaxial Strain in Graphene by Raman Spectroscopy: G Peak Splitting, Grüneisen Parameters, and Sample Orientation. *Phys. Rev. B: Condens. Matter Mater. Phys.* **2009**, *79* (20), 205433.
(42) Huang, M.; Yan, H.; Heinz, T. F.; Hone, J. Probing Strain-Induced Electronic Structure Change in Graphene by Raman Spectroscopy. *Nano Lett.* **2010**, *10* (10), 4074−4079.
(43) Yoon, D.; Son, Y.-W.; Cheong, H. Strain-Dependent Splitting of the Double-Resonance Raman Scattering Band in Graphene. *Phys. Rev. Lett.* **2011**, *106* (15), 155502.
(44) Mohr, M.; Maultzsch, J.; Thomsen, C. Splitting of the Raman 2D Band of Graphene Subjected to Strain. *Phys. Rev. B: Condens. Matter Mater. Phys.* **2010**, *82* (20), 201409.
(45) Frank, O.; Mohr, M.; Maultzsch, J.; Thomsen, C.; Riaz, I.; Jalil, R.; Novoselov, K. S.; Tsoukleri, G.; Parthenios, J.; Papagelis, K.; Kavan, L.; Galiotis, C. Raman 2D-Band Splitting in Graphene: Theory and Experiment. *ACS Nano* **2011**, *5* (3), 2231−2239.
(46) Sachs, B.; Wehling, T. O.; Katsnelson, M. I.; Lichtenstein, A. I. Adhesion and Electronic Structure of Graphene on Hexagonal Boron Nitride Substrates. *Phys. Rev. B: Condens. Matter Mater. Phys.* **2011**, *84* (19), 195414.
(47) Lee, J. E.; Ahn, G.; Shim, J.; Lee, Y. S.; Ryu, S. Optical Separation of Mechanical Strain from Charge Doping in Graphene. *Nat. Commun.* **2012**, *3* (1), 1024.
(48) Ott, A. K.; Ferrari, A. C. Raman Spectroscopy of Graphene and Related Materials. In *Encyclopedia of Condensed Matter Physics*, 2nd ed.; Academic Press, 2024; pp 233−247.
(49) Bosak, A.; Krisch, M.; Mohr, M.; Maultzsch, J.; Thomsen, C. Elasticity of Single-Crystalline Graphite: Inelastic x-Ray Scattering Study. *Phys. Rev. B: Condens. Matter Mater. Phys.* **2007**, *75* (15), 153408.

https://doi.org/10.1021/acs.jpcc.5c00506
J. Phys. Chem. C 2025, 129, 7508−7519